1

Main Medical Imaging Techniques

1.1. Introduction

The field of medical imaging has experienced revolutionary progress, with improved accuracy and reduced invasiveness. Medical imaging techniques make it possible to better understand human behavior and are essentially composed of an energy-emitting source able to penetrate the human body. During its penetration, this energy can be absorbed or attenuated at different levels depending on the tissue density and the penetrated atomic number. This process generates signals that can be detected by special detectors specific to the energy source. Mathematical models are then used to manipulate these signals in order to create medical images.

An imaging modality is a specific imaging technique or system used to visualize the inside of the body. According to the used energy source, several modalities can be distinguished. Diagnostic radiology is based on the use of the electromagnetic spectrum beyond the visible light region, such as X-rays used in mammography and computed tomography, whereas magnetic resonance imaging is based on the use of radiofrequencies and ultrasound imaging is based on the use of mechanical energy in the form of high-frequency sound waves.

During the acquisition of a medical image, the acquisition conditions and the technical quality of the image are the two determinant factors of its diagnostic utility. In general, the image quality involves compromises; it improves when the dose of X-rays increases in radiography and computed tomography, when the image acquisition time increases in MRI and when

the power levels increase in ultrasound imaging. However, the safety and the comfort of the patient are crucial parameters that should be taken into account during the acquisition process, and an excessive radiation dose should not be applied in pursuit of a perfect image. Indeed, the quality of the image and the safety of the patient must be balanced.

This chapter briefly addresses the four medical imaging modalities that are most commonly used to create FE models of different parts of the human skeleton: X-ray imaging, computed tomography (CT), magnetic resonance imaging (MRI) and ultrasound imaging.

1.2. X-ray imaging

X-ray imaging is the foremost technique that is used to perform medical imaging. The X-rays used in radiography were discovered in 1895 by physicist Wilhelm Roentgen, who created the first radiographic images of the human anatomy (Figure 1.1) (Bushberg and Boone 2011).

Hence, X-ray imaging has gone on to define the radiology field, leading to the emergence of radiologists and specialists in interpreting medical images (Bushberg and Boone 2011).

1.2.1. *Definition of X-rays*

X-rays fall within the electromagnetic rays (Figure 1.2) that transport radiating energies through space by waves and photons. These rays can be represented by a photon or a wave model and can be categorized according to their energy, frequency $\boldsymbol{f_p}$ or wavelength $\boldsymbol{\lambda_p}$ (Berger *et al*. 2018):

$$\boldsymbol{\lambda_p} = \frac{\boldsymbol{c_0}}{\boldsymbol{f_p}} \qquad [1.1]$$

where $\boldsymbol{c_0}$ denotes the wave propagation speed, i.e. the speed of light. The photon energy $\boldsymbol{E_p}$ ($\boldsymbol{eV}$) is directly linked to $\boldsymbol{\lambda_p}$ or to $\boldsymbol{f_p}$ as follows (Berger *et al*. 2018):

$$\boldsymbol{E_p} = \frac{\boldsymbol{hc}}{\boldsymbol{\lambda_p}} = \boldsymbol{f_p h} \qquad [1.2]$$

where $\boldsymbol{h}$ is Planck's constant ($\approx \mathbf{6,626069 \times 10^{-34}\ Js}$) and $\boldsymbol{c}$ is the speed of light ($\approx \mathbf{2,99792 \times 10^{5}\ m\ s^{-1}}$).

By passing through different materials, X-rays lose a certain amount of energy according to the absorption behavior of each material, which describes the basic principle of traditional X-ray radiography that measures the amount of lost energy. The contrast in the image comes from the difference in the energy amount lost between the different materials. The absorbed energy amount also depends on the dose released during acquisition (Berger *et al*. 2018).

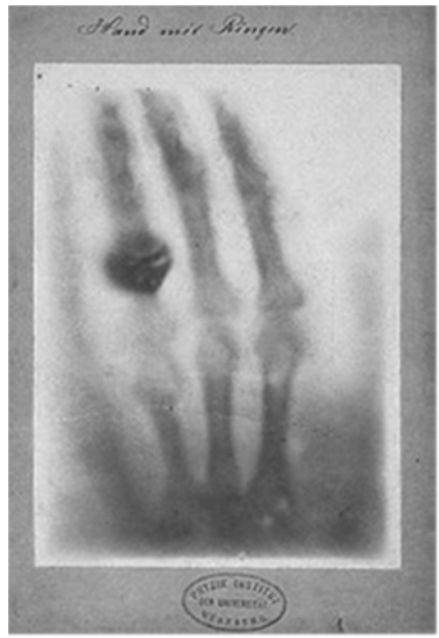

Figure 1.1. *This famous image represents the oldest existing human X-ray image. It was taken on December 22, 1895 by Roentgen, and shows the hand of his wife. This X-ray, clearly showing the bones of the hand as well as two rings on one of the fingers, represents the beginning of diagnostic radiology. Within several months, Roentgen was able to determine the physical properties underpinning X-rays and published, on December 28, 1895, his conclusions in a preliminary report entitled "On a New Kind of Rays" in the Proceedings of the Physico-Medical Society of Würzburg. On January 23, 1896, an English translation was published in the scientific journal* Nature, *and was quickly followed by the news of the discovery spreading around the world. Thanks to the medical applications of this kind of ray, radiological imaging has made rapid progress to become an essential part of medical care. The letter "X", assigned by Roentgen, indicates the unknown nature of these rays, hence the name "X-ray" (Gunderman 2012)*

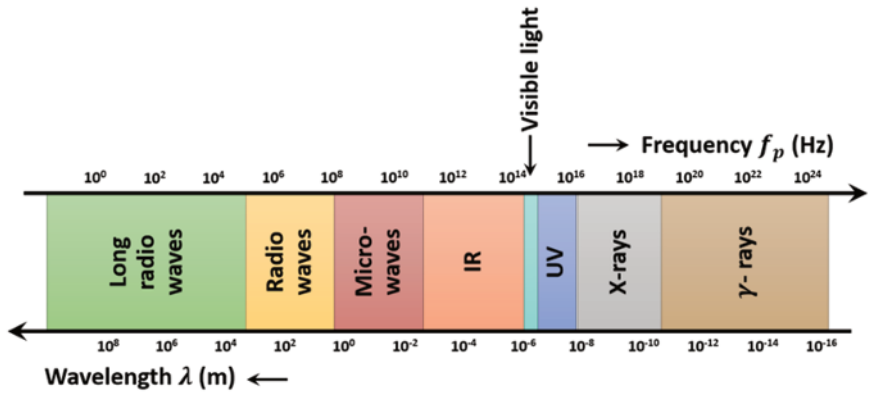

Figure 1.2. *Frequencies and wavelengths of the different types of electromagnetic rays. X-rays are spread across a wavelength ranging from* $0.01\ nm$ *to* $10\ nm$*, corresponding to an energy level of* $100\ KeV$–$100\ eV$ *(Berger* et al. *2018)*

1.2.2. *X-ray instrumentation and generation*

The X-ray tube is a glass vacuum tube with a cathode made of a tungsten filament and an anode that can be made of tungsten, molybdenum or rhodium (Figure 1.3). By heating the cathode filament, electrons are produced and released into the tube (Reilly 2019). Owing to the significant difference in potential between the anode and the cathode, the produced electrons are accelerated and hit the target element of the anode at a high speed. The incident electrons are deviated because of the magnetic field of the atoms composing the anode material, with a decrease in their speed, thereby generating X-rays. The direction of these rays is defined by the anode tilt angle (Berger *et al*. 2018).

The interaction between the high-energy electrons and the target element produces heat with a small amount of X-rays. The vacuum conditions make it possible to avoid any interaction between the electrons and gas molecules before reaching the anode. For the majority of diagnostic procedures using X-rays, the applied tension ranges from 40 to 150 kV, but it is lower for mammography (36–40 kV) (Delbeke and Segall 2011). The anode is therefore often made of tungsten due to its high melting point and high atomic number, which may increase the interaction rate and, as a result, the production of X-rays. In mammography, the anode can also be made of molybdenum or rhodium (Reilly 2019).

X-rays can be produced according to two different processes (Figure 1.4). An initial process corresponds to a relatively strong interaction between the electron emitted by the cathode and another electron from the inner layer of the anode atom, which results in a complete elimination of the electron from the inner layer, with its place taken by an orbital electron from the outer layer of the target atom. The transition from the outer layer to the inner layer is accompanied by the emission of X-rays with energy equal to the difference in the binding energies of the two involved orbital electrons. Characteristic radiation produces a discrete spectrum of typical peaks. A second process corresponds to an interaction between the electron emitted by the cathode and the nucleus of the anode target atom, generating a deviation and a decrease in the speed of this incident electron. This loss of kinetic energy is at the root of the production of Bremsstrahlung X-rays ("bremsen" in German means "to brake"), producing a continuous spectrum (Berger *et al*. 2018).

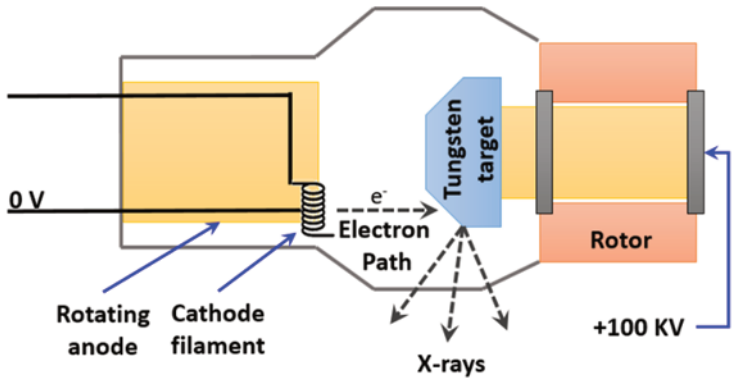

Figure 1.3. *An X-ray tube containing a cathode filament that, when heated, releases electrons accelerated because of a difference in the potential of* $100\ kV$ *towards an anode generally made of tungsten. The heat generated during this process can be cleared by rotating the anode. X-rays are produced as a result of the interaction of incident electrons with orbital electrons from the target tungsten atom nuclei (Reilly 2019)*

All low-energy photons are, in fact, absorbed by the human body as they do not have enough energy to pass through the body, and thus they never reach the detector. These photons thereby significantly increase the absorbed radiation dose during image acquisition without actually increasing its quality. As a result, a thin aluminum plate is placed between the X-ray

source and the human body, which acts as an X-ray filter (different from the mathematical filters used in image processing) (Berger *et al*. 2018). This aluminum filter is often completed by a second filter made of copper. The low-energy electrons are known as soft radiation, high-energy ones are called hard radiation, and the process of eliminating soft radiation is called beam hardening. The area of the human body to be irradiated is delimited by a collimator, and the dispersion photons are absorbed by a collimating scatter grid. The latter can be, for example, made of lead. It allows the passage of photons with a low incidence angle and blocks those with a high incidence angle. In pediatrics, the dispersion grid is not always used because of the limited dispersion in small children (Suetens 2009).

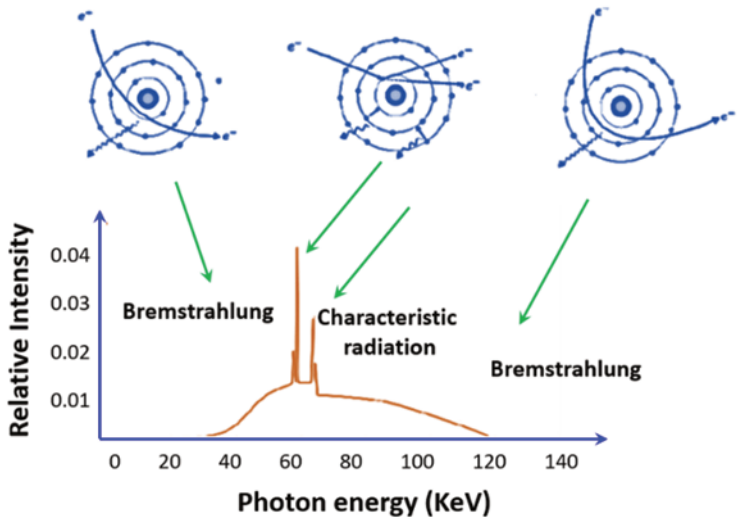

Figure 1.4. *X-ray spectrum from a tungsten tube showing the continuous spectrum produced by Bremsstrahlung and the peaks produced by the characteristic radiation (Berger* et al*. 2018)*

The X-rays reaching the detector make it possible to create medical images of the inside of the body for the area they have passed through. The detector may be (1) a cassette containing a storage plate, (2) an image intensifier coupled with a camera, (3) a screen–film combination, in which a film is sandwiched between two screens, (4) a flat panel active matrix detector, or (5) a dual layer detector (Suetens 2009).

Figure 1.5 shows a complete radiographic imaging system comprising: (1) an X-ray source, (2) an aluminum filter to remove low-energy photons and thus increase the average energy of the photon beam, a process called beam hardening, (3) a collimator limiting the area to be irradiated, (4) a patient attenuating the X-ray beam and causing dispersion, (5) a collimating scatter grid to absorb the dispersion photons, and (6) a detector (Suetens 2009).

In the radiographic image, tissues with high X-ray absorption, such as bones, are represented by light structures.

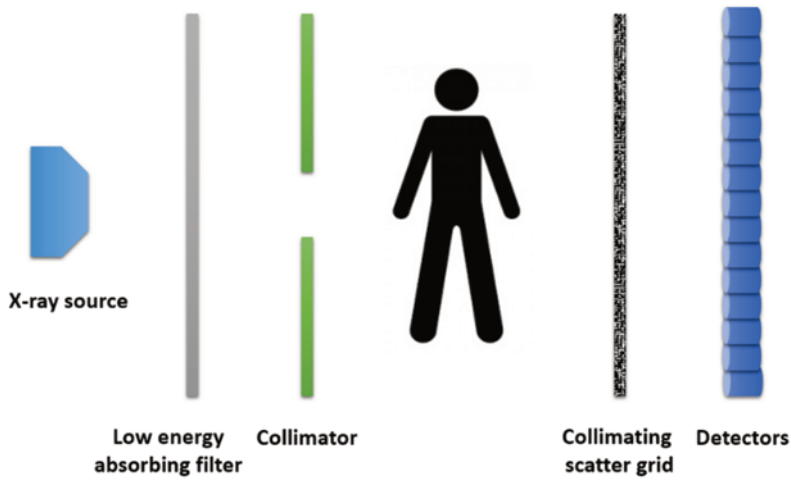

Figure 1.5. *Schematic representation of the radiographic imaging system (Suetens 2009)*

1.2.3. *Applications of X-ray imaging*

X-ray imaging is used in several applications. The most common applications are listed below.

1.2.3.1. *Conventional radiography*

Conventional radiography refers to the process of creating 2D images using X-ray projection, by measuring the attenuation of those rays as they pass through the body. Therefore, this technique is mainly used to examine fractures and changes in the skeletal system due to the high attenuation coefficient of bones compared to that of the surrounding tissue, which

provides a good contrast (Figure 1.6) and an accurate detection, as well as a distinct classification of different fractures (Berger *et al*. 2018). Moreover, radiography is frequently used to accurately measure bone mineral density, making it possible to assess and monitor the risk of osteoporosis (Shi *et al*. 2016), and is considered as the primary screening method for detecting bone tumors and tumor-like lesions (Morrison *et al*. 2013). In addition, this imaging modality is able to provide information on lesion location, internal matrix, margins and associated periosteal response, and thus make it possible to guide differential diagnosis (Wu and Hochman 2012). Using radiography, a single image or a small number of images can be acquired for a specific view.

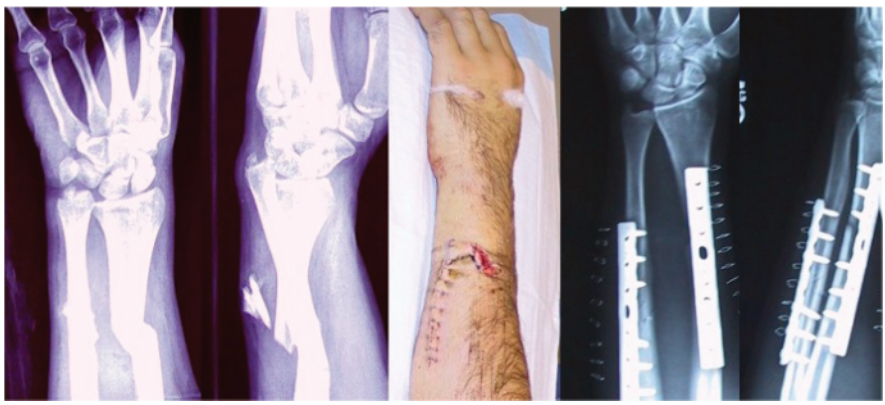

Figure 1.6. *Radiographic images showing (left) fractures in the forearm and (right) metal plates used to fix the ulna and the radius (Berger* et al. *2018). For a color version of the figure, see www.iste.co.uk/benkahla/finite.zip*

1.2.3.2. *Dual energy X-ray absorptiometry*

Dual-energy X-ray absorptiometry (DXA or DEXA), also known as bone densitometry, is an imaging modality subtracting two images obtained using different X-ray spectra (Flower 2012). It is based on two concepts: (1) the passage of two X-ray beams or an X-ray beam of two different energies through the body or the region of interest, and (2) the attenuation of the calculated beam or beams, since the emitted photon number is known (Ahmad *et al*. 2014). The attenuation (absorption or dispersion) of the X-ray beam varies with the energy intensity, as well as with the human tissue

thickness and density. It decreases as photon energy increases and increases as tissue thickness and density increase (Ceniccola *et al*. 2018). For example, the attenuation is more important in bone tissue than in soft tissue (Guglielmi *et al*. 2016).

In fact, this modality makes it possible to estimate the value of the attenuation coefficient R related to two different energy levels. The value of R is constant for bones and fats, but variable for soft tissues in accordance with their composition (the higher the percentage of fat in the soft tissue, the lower the values of R) (Ceniccola *et al*. 2018). Assuming that the body is subdivided into three groups: bone, lean tissue and adipose tissue, DXA provides measurements of the mineral content, lean mass and fat mass of the body or the region of interest, without directly measuring these three components (Kendler *et al*. 2013; Ahmad *et al*. 2014; Bazzocchi and Diano 2014). The amount of fat mass and lean mass is inferred on the basis of the ratio of fat mass to lean mass at the boneless neighboring pixels, thereby assuming that the amount of fat at the bone level is similar to that at the adjacent boneless tissues (Bazzocchi *et al*. 2014).

In accordance with the amount of radiation reaching the detector and the two different energies used simultaneously, a gray value with two different attenuation values is assigned to each pixel. In the case of bone, both attenuation values provide information on bone mineral content that, when divided by the bone surface, make it possible to determine bone mineral density (Lucas *et al*. 2017). The attenuation itself can be subdivided owing to photoelectric absorption and photon dispersion. These two components have different energy dependence, because of which a photoelectric component and a dispersion component can be extracted from the two initial images. Similarly, the difference in the amounts of photoelectric dispersion and absorption between different materials makes it possible to create images of the thicknesses of two selected materials. By combining these thicknesses, the attenuation maps recorded in the two original images may be reproduced. Therefore, an appropriate selection of these materials makes it possible to create images showing or eliminating any type of tissue, as desired (Figure 1.7). For example, images of bone structure and soft tissue can be separately viewed by selecting the bone and the tissue (with a nominal composition) as base materials (Flower 2012).

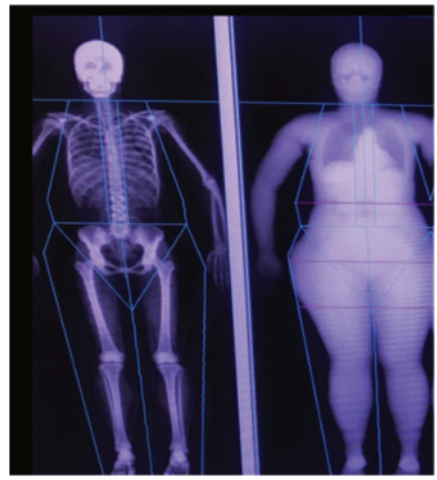

Figure 1.7. *Image of a DXA examination (Ceniccola* et al. *2018). For a color version of the figure, see www.iste.co.uk/benkahla/finite.zip*

DXA was originally developed to measure bone mineral density and is frequently used to diagnose osteoporosis. This modality is currently the reference technique in body composition analysis at the molecular level, which is recognized for the accuracy of its measurements for a specific region of interest or for the whole body (Marinangeli and Kassis 2013; Guglielmi *et al*. 2016). With the latest generation of densitometers, body composition can be assessed using a single whole body scanner, which consequently reduces the duration of radiation exposure and acquisition time. The obtained images are comparable to the radiological images and provide accurate data (Bazzocchi *et al*. 2014; Ceniccola *et al*. 2018).

1.2.3.3. *Fluoroscopy*

Fluoroscopy is a transmission projection imaging modality, making it possible to periodically obtain X-ray images at a certain frequency, which is equivalent to a real-time radiography (Bushberg and Boone 2011). The frame rate depends on the acquisition speed of the detection system, which may reach almost 30 frames per second. Image intensifiers and FPD screens are potential detection systems (Berger *et al*. 2018).

Fluoroscopy is used in minimally invasive therapeutic procedures, requiring real-time image feedback to guide the used tools, such as endoscopes or catheters, without direct visual contact with the intervention

area (Figure 1.8). It makes it possible to visualize the gastrointestinal tract and vessels using contrast agents, and can provide radiographic films of anatomical movement, such as those of the esophagus or heart (Bushberg and Boone 2011; Berger *et al*. 2018).

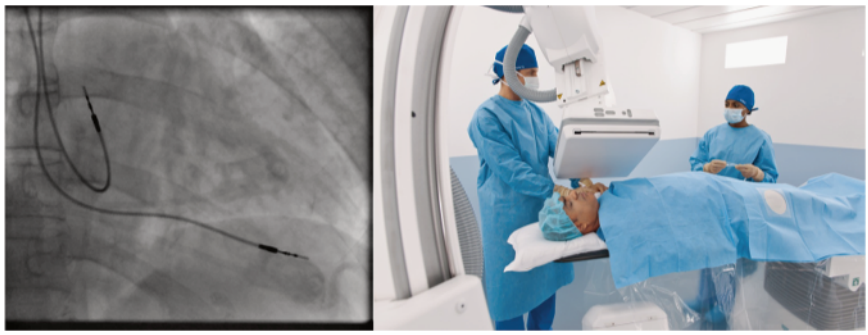

Figure 1.8. *Image of a fluoroscopy sequence while introducing two pacemaker electrodes (left). Typical clinical configuration of a minimally invasive surgical procedure guided by a fluoroscopy sequence using a freely positioned device, with the X-ray source placed under the patient and the FPD right above him (right) (Berger* et al. *2018)*

1.2.3.4. *Digital subtraction angiography*

Owing to the poor contrast of X-ray imaging between the vessels and the surrounding tissue, digital subtraction angiography (DSA) is used to visualize the gastrointestinal tract and blood vessels using a contrast agent that can be whether swallowed or injected into the bloodstream, in order to obtain information about the size, shape, flow or light of the target area. Barium and iodine are two typical contrast agents, with the first being used for gastrointestinal examinations and the second for intravascular examinations (Flower 2012; Berger *et al*. 2018).

Figure 1.9 shows the stages of angiography obtained by acquiring an image of the region of interest without a contrast agent, and then by acquiring another image during the transit of the contrast agent. By subtracting the image showing the surrounding tissue from the image showing the tissue and the vessels, the attenuation caused by the contrast agent can then be measured and the resulting angiogram clearly shows the blood vessels in the region of interest. Two further examples of DSA are shown in Figure 1.10.

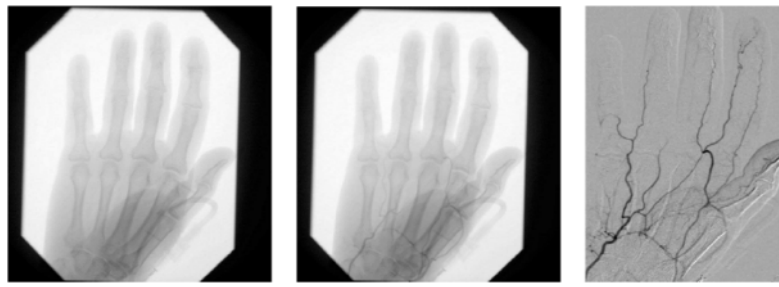

Figure 1.9. *Creation of a DSA, starting by creating an image of the hand without any injected contrast agent, known as a mask image (left), followed by the creation of a fill image of the same hand after injecting a contrast agent into the vascular system (center). The subtraction of the two images provides the angiogram (right), which only shows the contributions of the contrast agent and, thereby, visualizes the vessels in the hand (Berger* et al*. 2018)*

Temporal and spatial filters can be used on all images to improve the signal-to-noise ratio (SNR) in the subtracted image, and corrections can be made to adjust for the movements of the patient (Flower 2012).

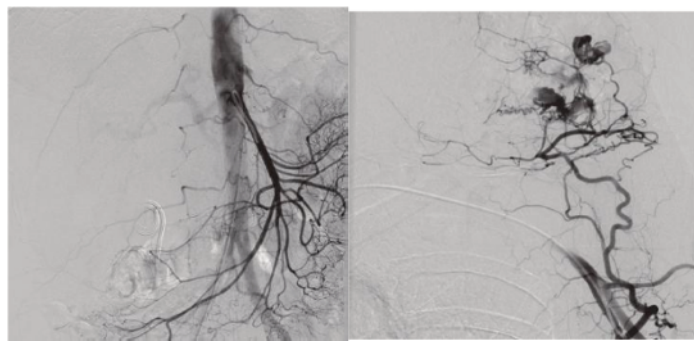

Figure 1.10. *Two examples of DSA. The left angiogram refers to the upper mesenteric artery feeding the intestines, with an anterior–posterior projection from the upper abdomen; the catheter is introduced into the aorta line. The right angiogram refers to one of the arteries feeding a hemangioma of the left trapezius of the shoulder, with an anterior–posterior projection of the left lung and shoulder; the catheter is introduced into the left subclavian artery (Flower 2012)*

1.2.3.5. *Mammography*

Mammography is an imaging modality specifically used to image the breast using X-ray projection, with energies much lower than those used in general radiography, making it possible to accentuate the contrast in the

breast in order to detect breast abnormalities, such as calcifications or masses. The used systems and detectors are therefore designed to particularly produce high quality images based on low X-ray doses. Mammography can be either (1) diagnostic, facilitating the diagnoses of women with breast symptoms, such as lumpiness, or (2) screening, making it possible to detect breast cancer in asymptomatic women (Figure 1.11A). Digital mammography enables computer-assisted detection, with which some systems provide a rotational movement of approximately 7 deg to 40 deg of the X-ray tube (and in some cases of the detector) around the breast, thereby producing a tomosynthesis (Figure 1.11B), with images parallel to the detector plane and capable of reducing the overlap of the anatomy below and above the plane in focus (Bushberg and Boone 2011).

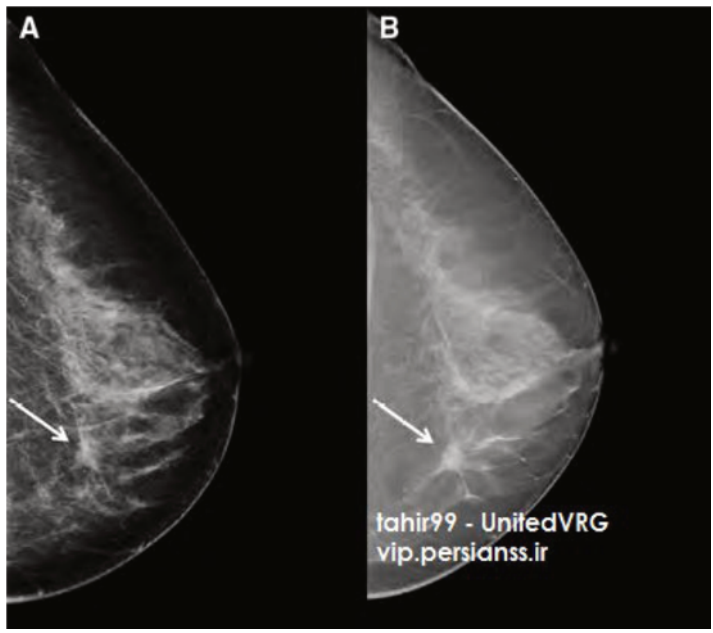

Figure 1.11. *(A) Digital mammogram showing the skin line of the breast, the fat tissue and a possible cancerous mass, indicated by the arrow. In projection mammography, tissue superposition at different depths can mask the malignancy characteristics or cause artifacts mimicking tumors. (B) Tomogram synthesized at mid-depth. By reducing the anatomy underlying and overlying the tomosynthesis, the suspicious mass in the breast is clearly represented with a spiculated appearance, indicative of cancer. Owing to its high sensitivity, very high benefit/risk ratio and low cost, X-ray mammography is currently the procedure of choice for screening and early detection of breast cancer (Bushberg and Boone 2011)*

1.2.4. *Advantages and disadvantages of X-ray imaging*

Table 1.1 summarizes the advantages and disadvantages of X-ray imaging.

Advantages	Disadvantages
Fast execution	Inadvisable during pregnancy
Non-invasive technique	Largely ineffective in distinguishing between different fat types (visceral, intramuscular and subcutaneous)
Low cost	Difficult to carry out for sick people or very small children who are unable to keep their back extended
Low radiation levels	Operation requires specific technical skills, as well as experience
Safe in repeated measurements	
Effective characterization of bone lesions and primary bone tumors	

Table 1.1. *Advantages and disadvantages of X-ray imaging (Ceniccola* et al. *2018)*

1.3. Computed tomography

Computed tomography (CT) is also an imaging technique that uses X-rays, based on the same physical principles as the X-ray imaging technique mentioned above: X-rays pass through the body or the region of the body to be scanned, and are attenuated according to the physical properties of the tissues through which they pass. Unlike "simple" X-ray techniques, CT makes it possible to create tomographic images, where "tomography" refers to an image (graphic) of a slice (tomo). One of the first scanners was composed of a single X-ray emitter with a single in-line detector, capable of rotating around the body or the region being scanned. The individual, who is in the tube containing the transmitter and detector, moves one centimeter or more through the tube after obtaining each slice in order to acquire the next slice. This process is repeated until scanning the whole region of interest, enabling the acquisition of a series of CT scans of that region. The number of transmitters and detectors has changed with the progressive development of this imaging technique, making it possible to obtain a 3D reconstruction and create cross-sectional views of the body or the region of interest. The use of CT dates back to the early 1970s and represents the first computer-assisted medical imaging modality, due to which the rate of exploratory surgery has been significantly reduced (Bushberg and Boone 2011; Miller *et al*. 2014).

1.3.1. *Description of the technique*

Fundamentally, a scanner measures the attenuation of a well-collimated X-ray beam along a line between the emission source and the detector. The body or region of interest is analyzed by the source–detector assembly, carrying out a linear translation movement. By rotating the X-ray tube around the body and combining X-rays from different angles, CT scanners produce a 3D replication of the body or region of interest. A numerical value, called CT value, is assigned to each voxel of the generated image, making it possible to measure the attenuation of body tissues in Hounsfield units (HU), using a standard scale for a linear attenuation coefficient and defining water as $\mathbf{0}\ \boldsymbol{HU}$ and air as $\mathbf{1000}\ \boldsymbol{HU}$ (Prado and Heymsfield 2014; Fosbøl and Zerahn 2015; Yip *et al*. 2015; Lucas *et al*. 2017; Ceniccola *et al*. 2018). The CT value is expressed as follows (Vogl *et al*. 2016):

$$\boldsymbol{CT} = \mathbf{1000}\left(\frac{\boldsymbol{\mu}-\boldsymbol{\mu_{H_2O}}}{\boldsymbol{\mu_{H_2O}}}\right) \qquad [1.3]$$

where $\boldsymbol{\mu}$ is the linear attenuation coefficient and $\boldsymbol{\mu_{H_2O}}$ is the linear attenuation coefficient of water. Using the HU scales, body tissues and organs can be determined by quantifying the muscle mass ($\boldsymbol{HU} = \mathbf{-29}$ to $\mathbf{+150}$), the subcutaneous and intramuscular fat tissue ($\boldsymbol{HU} = \mathbf{-190}$ to $\mathbf{-30}$), as well as the visceral fat tissue ($\boldsymbol{HU} = \mathbf{-150}$ to $\mathbf{-50}$). For each image, the cross-sectional area of the different tissues (Figure 1.12) can be determined manually or using a software (Ceniccola *et al*. 2018).

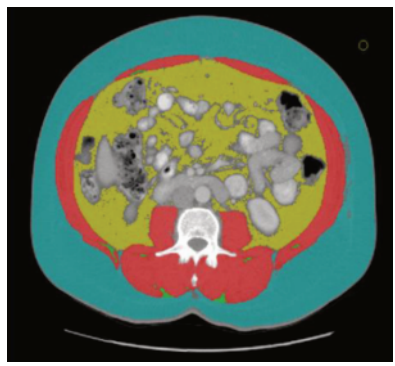

Figure 1.12. *Cross-section of the abdominal segment showing the third lumbar vertebra with different colored tissues: skeletal muscle in red, visceral adipose tissue in yellow, subcutaneous adipose tissue in blue and intramuscular adipose tissue in green (Ceniccola* et al. *2018). For a color version of the figure, see www.iste.co.uk/benkahla/finite.zip*

1.3.2. *Development of computed tomography*

The first CT system was built in 1971 by Sir Godfrey Newbold Hounsfield and Allan McLeod Cormack, and was used to carry out the first clinical scan (Figure 1.13) in the same year. This seminal invention enabled them to win the Nobel Prize in Medicine in 1979. In 1990, the helical scanning system was introduced by Willi Kalender and his colleagues, and was named for its helical trajectory during image acquisition. The first scanners were characterized by a relatively long data acquisition time, with the reconstruction of a single 2D slice, a slow quantification and a low spatial resolution. In 2002, the quantification depth, the spatial resolution and the rotation speed of the system were considerably improved, with the ability to obtain up to **16** slices in parallel. In recent years, spatial and temporal resolutions have been continually improved, and the integration of two X-ray emission sources into a single scanner in 2005 was an important step. The use of these two sources with different voltages, equivalent to a double energy scan, can considerably increase the acquisition rate, as well as the slice number acquired at the same time. Hence, the field of view in the axial direction has also increased with voxel sizes less than one millimeter. It has therefore become possible to scan an entire organ with a single rotation, which significantly reduced movement artifacts. Today, CT is one of the most important medical imaging technologies, providing advantageous and fascinating views of the human body (Figure 1.14) (Flower 2012; Maier *et al*. 2018).

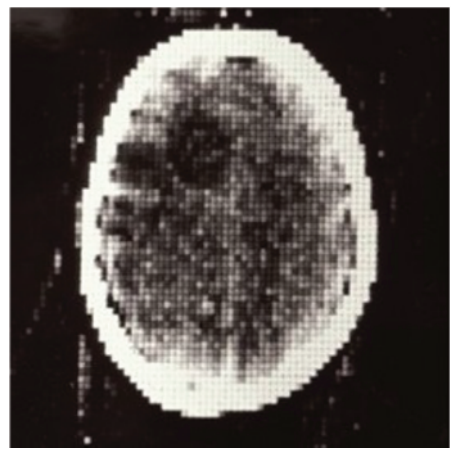

Figure 1.13. *First clinical CT scan obtained in October 1971 at Atkinson Morley hospital in London (Maier* et al*. 2018)*

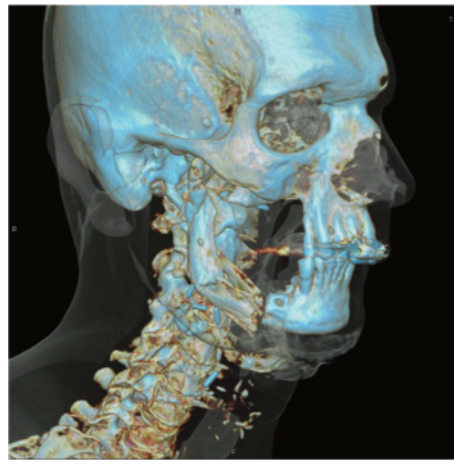

Figure 1.14. *Volume-rendered CT scan of the head (Maier* et al. *2018). For a color version of the figure, see www.iste.co.uk/benkahla/finite.zip*

1.3.3. *Instrumentation*

Seven scanner generations have been developed over time to improve overall performance, mainly for the duration of data acquisition.

1.3.3.1. *First-generation scanners*

Although first-generation (1G) scanners are no longer manufactured for medical imaging, their geometry is still useful for understanding the theoretical ideas behind image reconstruction. 1G scanners have a single finely collimated source, emitting a pencil-shaped X-ray beam, with a single detector, all of which moves in linear and circular motions around the body, performing a "translation–rotation" movement (Gupta *et al*. 2013; Prince and Links 2015). Initially, the source–detector assembly takes a linear step around the individual, allowing parallel projections to be measured, one sample at a time. After each projection, it rotates at a certain angle to make the next projection (Figure 1.15). The presence of a single detector allows easy calibration with relatively low costs. Owing to 2D collimation at the source, as well as with the detector, 1G scanners are characterized by a higher dispersion rejection than any other generation. The acquisition time is very slow, even for acquiring relatively low resolution images (Flower 2012).

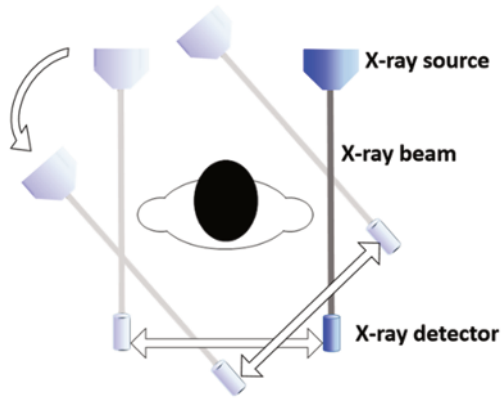

Figure 1.15. *Geometry of a 1G scanner (Prince and Links 2015)*

1.3.3.2. *Second-generation scanners*

Second-generation (2G) scanners are also no longer used in medical imaging. They consist of a single source and a network of detectors arranged along a line or in a circle (Figure 1.16). The source and detectors also move in a "translation–rotation" movement in the same way as in 1G scanners, but the X-ray beam is fan-shaped, maintaining the energy in the section while having distributed it over the detector network. The central detectors thereby detect the projection in a similar manner to detectors in 1G scanners, but the additional detectors allow further projections to be obtained at different angles (Prince and Links 2015).

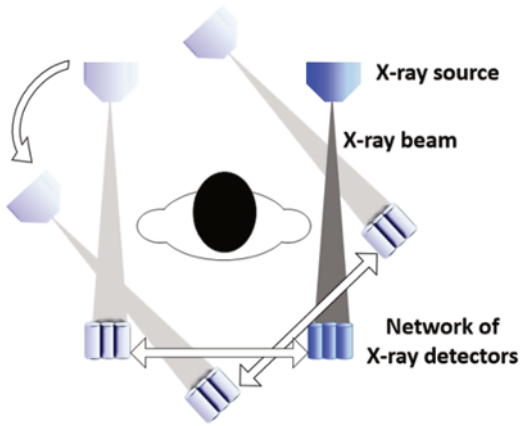

Figure 1.16. *Geometry of a 2G scanner (Prince and Links 2015)*

1.3.3.3. *Third-generation scanners*

Third-generation (3G) scanners are systems that rotate continuously by means of a sliding slip ring for power supply and data collection. This generation of scanners has of a single X-ray emission source and a network of detectors, with a sufficiently wide fan beam to cover a complete cross-section of the patient (Figure 1.17). The source–detector unit performs only synchronized "rotation–rotation" movements without the need for linear scanning (Aichinger *et al*. 2011; Adam *et al*. 2014).

1.3.3.4. *Fourth-generation scanners*

Fourth-generation (4G) scanners have a single rotating X-ray source and a set of fixed detectors arranged in a ring. X-rays are emitted in a fan beam wide enough to cover the cross-section of the patient's body. Each detector therefore receives energy from the source moving around the patient, with small gaps separating the detectors and allowing X-rays to escape (Figure 1.18). This generation of scanners is characterized by more efficient detection than 3G scanners; however, the image quality of both generations is comparable owing to the likelihood of the detectors to scatter, since collimation cannot be used with 4G scanners. The image display is almost instant due to the high rotational speed of the X-ray emission source; however, the design has been abandoned owing to a number of problems, namely the extent of dispersion artifacts (Flohr 2013; Prince and Links 2015).

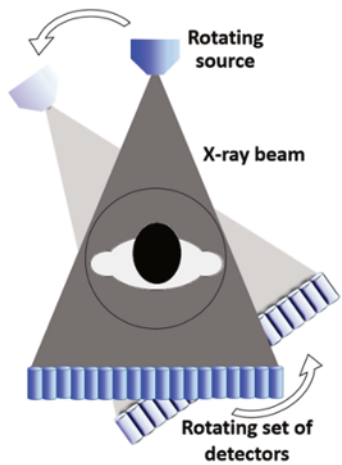

Figure 1.17. *Geometry of a 3G scanner (Prince and Links 2015)*

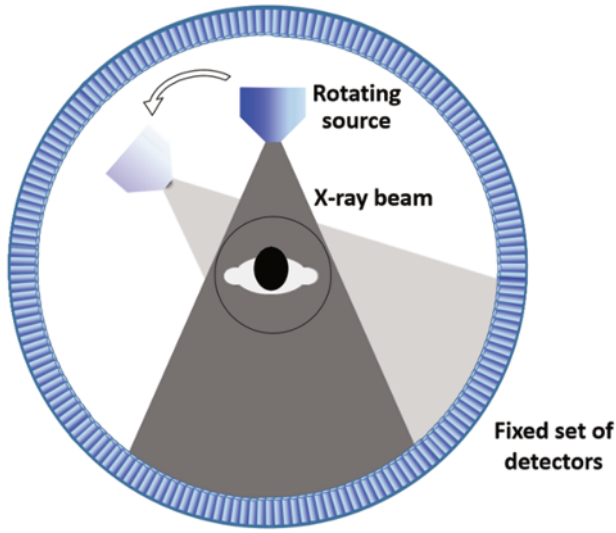

Figure 1.18. *Geometry of a 4G scanner (Prince and Links 2015)*

1.3.3.5. *Fifth-generation scanners*

Fifth-generation (5G) scanners, also known as "electron beam computed tomography" (EBCT), are based on the use of an accelerated electron beam in a funnel-shaped vacuum tunnel. Deflection coils, organized in a semi-circular configuration and placed beneath the patient, deflect these electrons electromagnetically onto targets corresponding to four tungsten anode bands surrounding the individual's body. X-rays are thereby generated in a fan-shaped beam, captured by a semi-circular detector located around the patient (Prince and Links 2015; Vogl *et al*. 2016). EBCT scanners are characterized by the very short acquisition time needed for the thicknesses of the individual layers, virtually eliminating movement artifacts. However, the image generated is of a poor quality owing to the loud noise and improving it requires longer acquisition times, with an increase in the radiation dose (Vogl *et al*. 2016).

1.3.3.6. *Sixth-generation scanners*

Sixth-generation (6G) scanners generally refer to helical scanners (Figure 1.19), although most scanners are nowadays able to perform a helical scan. Based on the same arrangement of the source–detector unit as that of 3G and 4G scanners, helical scanners consist of moving the patient table

perpendicular to the source–detector plane, while maintaining the rotation of the X-ray emission source. This creates a helical movement around the body, making it possible to acquire a continuous volume of data during a single breath of the patient. As a result, the acquisition rate is considerably improved and the artifacts are significantly reduced. This acquisition technique provides a retrospective reconstruction of several superimposed slices, thereby improving small lesion visualization and allowing the creation of a very detailed 3D CT angiogram (Klein *et al*. 2018).

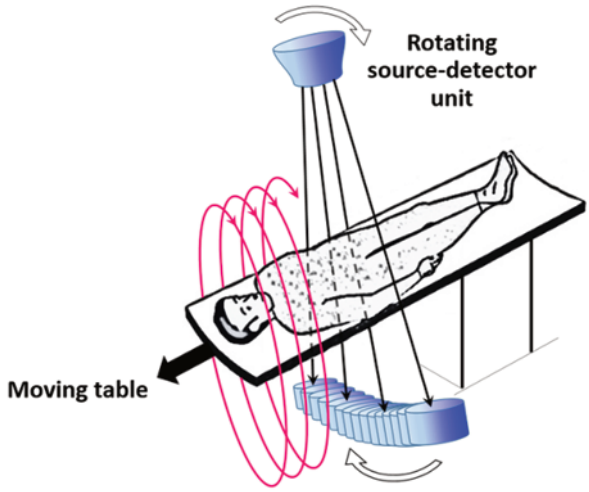

Figure 1.19. *Geometry of a 6G scanner or helical scanner (Aichinger* et al. *2011)*

1.3.3.7. *Seventh-generation scanners*

Seventh-generation (7G) scanners emerged following the advent of multidetector CT (MDCT) scanners. As their name indicates, these scanners use several axial rows of parallel detectors that collect a thick fan-shaped X-ray cone beam (Figure 1.20). Because of this conical shape and the typical enlargement of the region of interest located in the center of the field of view, the detector rows are approximately twice as wide as the minimum available cross-section thickness. This geometry makes it possible to simultaneously collect a large number of one-dimensional projections (Adam *et al*. 2014; Prince and Links 2015). MDCT scanners are characterized by a short sampling period with a reduction in movement artifacts, which can be very useful for children, seriously ill patients and victims of accidents. Longer examination sections may be used to trace the

vessels. Isotropic imaging can be carried out with finer collimation, which is particularly advantageous for visualizing the musculoskeletal system and temporal bone with multi-plane reconstructions (Vogl *et al*. 2016).

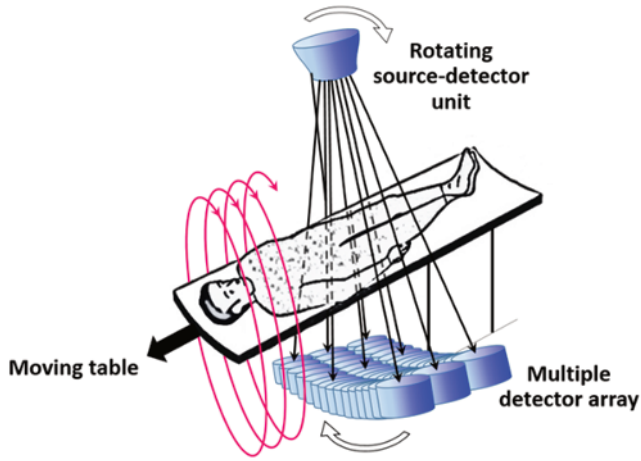

Figure 1.20. *Geometry of a 7G scanner or MDCT scanner (Adam* et al. *2014)*

The first four generations of CT scanners are characterized by the use of a single X-ray source, as it is expensive, large and must be constantly calibrated. In addition, rotating a large object (source and/or detectors) limits the overall imaging speed. However, new data processing procedures and methods must be developed in view of the emergence of helical and MDCT scanners.

1.3.4. *Applications*

1.3.4.1. *Computed tomography fluoroscopy*

CT fluoroscopy is a real-time imaging technique that considerably improves the capacity and speed to carry out image-guided percutaneous interventions, while applying a moderate radiation dose. Images are quickly reconstructed, with the scanning table displaced to observe anatomy and lesions, as well as catheter and needle placement in real time. This imaging technique is frequently used to guide operations through the body, in addition to drainage and biopsy procedures. It is particularly used to guide

the placement and movement of needles or catheters in moving organs, such as the abdomen or chest (Klein *et al*. 2018).

1.3.4.2. *Perfusion computed tomography*

Perfusion CT imaging is based on the use of contrast attenuation curves in tissues, as well as in their afferent and efferent vessels, allowing the measurement of blood volume, flow and transit in tissues, in addition to blood vessel leakage. A rapid intravenous bolus injection is performed, and the data from the same region of interest is obtained in succession. Hence, perfusion CT represents a multi-phase imaging modality, with a reduction in the radiation dose during each phase to avoid excessive exposure to radiation. It is particularly used for diagnosing strokes (Adam *et al*. 2014) (Figure 1.21), and is increasingly used in oncology to examine the anti-angiogenic treatment effects at the early stage of clinical trials (García-Figueiras *et al*. 2013). Two main methods of image analysis have been described: (1) the first, more robust method is based on contrast slope improvement, requiring high injection rates but not able to provide absolute measurements, and (2) the second method is more susceptible to noise and inconsistencies in data, but able to provide absolute values based on Fourier deconvolution methods (Adam *et al*. 2014).

1.3.4.3. *Dual-energy computed tomography*

Dual-energy, or double-source, CT is an imaging technique that uses two sources and two detectors of X-rays, in order to determine the behavior and composition of the target tissue at different radiation energies. Differences in soft tissue and fat tissue, as well as contrast agents, at different energy levels, increase lesion visibility and characterization. Data acquisition time can be half the time needed when using conventional MDCT, which significantly improves the ability to visualize certain organs, such as the heart, without using potentially dangerous heart rate depressant substances. Dual-energy CT can also be used to determine urinary stone chemical composition and to select appropriate medical or surgical treatment (Klein *et al*. 2018). Moreover, it can help to accurately and sensitively distinguish hemorrhage from iodinated contrast agent staining that may occur after an endovascular thrombectomy in cases of infarction (Figure 1.22) (Gupta *et al*. 2010).

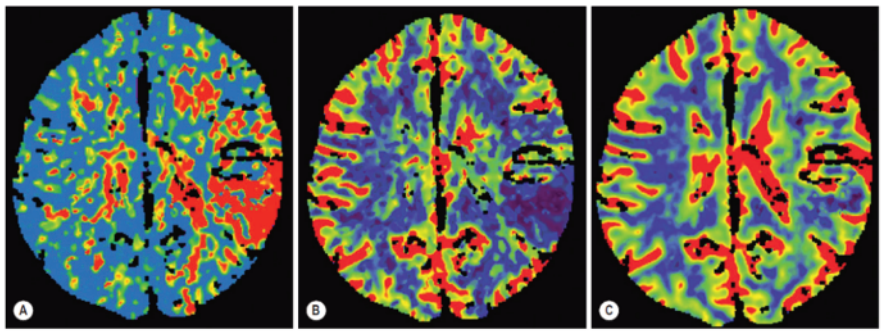

Figure 1.21. *Perfusion CT showing an infarct of the left middle cerebral artery territory. The mean transit time map (A) shows an area of delayed mean transit time in the posterior part of the left middle cerebral artery territory. The cerebral blood flow map (B) shows a larger area of cerebral blood flow revealing ischemic and infarcted tissues. The cerebral blood volume map (C) shows a small area of reduced cerebral blood volume in the left parietal convexity corresponding to core infarct. The area of incompatibility between the reduced cerebral blood flow and cerebral blood volume regions is a potentially salvageable ischemic penumbra (Adam* et al*. 2014). For a color version of the figure, see www.iste.co.uk/benkahla/finite.zip*

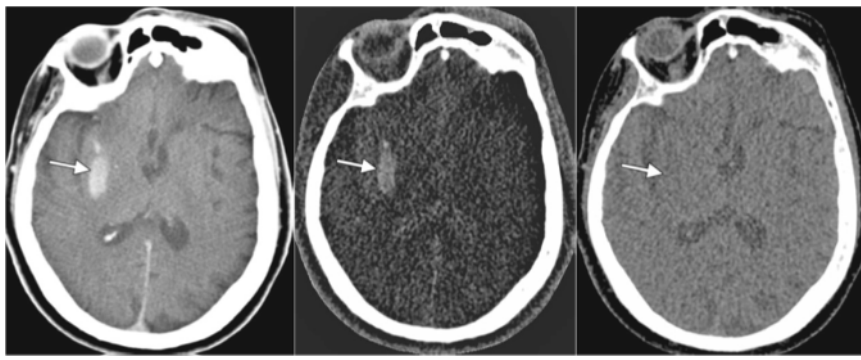

Figure 1.22. *Dual-energy CT showing (left) a single-energy axial CT scan, (middle) a corresponding iodine superimposition image indicating hyperattenuation at the left frontal lobe and caudate nucleus (arrows), and (right) a virtual non-contrast image indicating the absence of hyperattenuation (arrow) and the presence of contrast staining rather than hemorrhage (Peh 2014)*

1.3.4.4. *Movement analysis*

The increasing width of the scanner detectors allows the evaluation of motion effects, due to the possibility of acquiring a large amount of data from the region of interest, either continuously or with very short time intervals. This technique is particularly used to assess tarsal or carpal joint instability, as well as to perform functional examinations of arterial compression syndromes (Adam *et al*. 2014).

1.3.5. *Advantages and disadvantages of computed tomography*

Table 1.2 summarizes the advantages and disadvantages of CT imaging technique.

Advantages	Disadvantages
Cross-section view	Contrast allergy
Tissue contrast	Relatively high cost
High-resolution image	High exposure to radiation
Rapid acquisition	Image analysis requiring technical skills
High quantitative and qualitative precision	Convenience sampling
Possibility of determining tissue quality	

Table 1.2. *Advantages and disadvantages of CT imaging techniques (Ceniccola* et al. *2018)*

1.4. Magnetic resonance imaging

Magnetic resonance imaging (MRI) is currently a major technique in the field of medical imaging, using magnetic fields about 10–60 thousand times stronger than the magnetic field of Earth (Bushberg and Boone 2011). This imaging technique is based on the principle of nuclear magnetic resonance (NMR), which enables imaging the nuclei of atoms, such as hydrogen, carbon, nitrogen, sodium and phosphorus, located inside the body (Miller *et al*. 2014). In most clinical cases, the used MRI focuses on imaging hydrogen nuclei (1H), since hydrogen is the most abundant atom in the human body, providing a relatively large magnetic moment. Indeed, the number of hydrogen atoms in the body exceeds 10^{27} (Maier *et al*. 2018) and a typical MRI voxel contains about 10^{21} (Haidekker 2013). NMR was first

reported in 1946 and its use as an *in vivo* imaging technique, now known as MRI, dates back to the early 1970s. Conventional NMR was first used to study the chemical content of material. The development of modern MRI machines has since allowed the acquisition of a detailed depiction of the human body and the various contrasting soft tissues, representing a very important step forward in the field of medical imaging in the 20th Century (Miller *et al*. 2014; Maier *et al*. 2018).

1.4.1. *Instrumentation*

The magnetic resonance system mainly consists of two equipment groups. The first is the control center, which is composed of a "host" computer with its graphical user interface. The associated electronic components and power amplifiers are generally located in an adjacent room and connected to the second equipment group. The latter is housed in the machine in which the patient is located (Figure 1.23), and includes the components generating and receiving the magnetic resonance signal, comprising a set of main magnetic coils, three gradient coils, compensation coils, as well as an integrated radiofrequency (RF) transmitter coil (Ridgway 2010). In order to use RF electromagnetic waves, or radio waves, the room containing this second equipment group must block potential electromagnetic noise sources and isolate them from its own RF. The magnet and its associated coils are therefore enclosed in a special examination copper-lined room, forming what the physics community calls a Faraday cage.

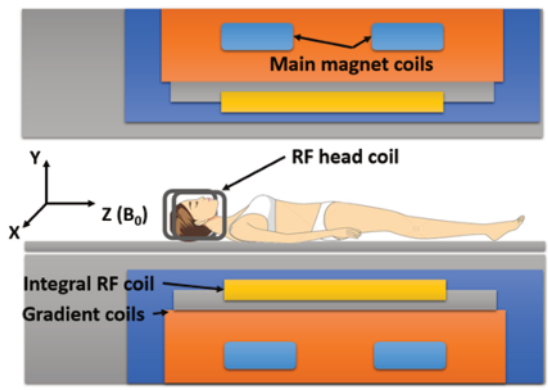

Figure 1.23. *Schematic representation of the relative positions of the different magnetic coils composing the magnetic resonance machine (Currie* et al. *2013)*

To obtain MRIs, the individual is placed in the magnetic field and subjected to RF pulses generated by the surrounding coils. These pulses are absorbed by positively charged hydrogen atoms of the patient (protons) and re-emitted to be detected by the coils surrounding the body. Absorption and re-emission are separated by a time period characteristic of each tissue. By slightly modifying the applied external magnetic field intensity according to the subject position, the resonance frequency of the proton of interest varies. The frequency and phase of the re-emitted RF pulses determine the position of each signal emitted from the body. The images produced by MRI represent slices of the body or region of interest, in which each point of the image depends on the micro-magnetic properties of the corresponding tissue (Bushberg and Boone 2011).

1.4.2. *Generation of the resonance effect*

The hydrogen atom nucleus has an intrinsic property called spin, corresponding to the rotation of its unique proton around an axis, which provides a magnetic effect (Figure 1.24). In the absence of an external magnetic field, the axes of the hydrogen nuclei are randomly oriented, i.e. the spin distribution will be random and the net macroscopic magnetic moment is null (Figure 1.25). When applying a magnetic field, $\vec{B}_0$, the water in the body becomes polarized, and the spins undergo a torque that aligns them in the same direction as the external magnetic field, $\vec{B}_0$, in the same way as a compass needle gradually aligns itself in the direction of this field. This alignment briefly activates an RF electromagnetic field, which in turn generates the rotation of the axes around the magnetic field direction, in the same way that the tilt of a spinning-top rotates around the gravity direction. It should be recalled that an RF wave corresponds to the variation of a magnetic field over time (Feeman 2010; Miller *et al*. 2014; Maier *et al*. 2018). RF waves are emitted at the same oscillation frequency as the hydrogen atoms; they disappear when their axes of rotation reach a stable position and are emitted again when these atoms are re-unbalanced (Maier *et al*. 2018).

Figure 1.24. *Representation of the hydrogen atom nucleus rotating (spinning) as it begins to have a magnetic effect (Maier* et al. *2018)*

The spin orientation may be parallel, i.e. in the same direction as the applied magnetic field, or antiparallel, i.e. in the opposite direction. Because the parallel orientation requires a lower energy level, more spins are oriented parallel than antiparallel to the magnetic field, and the difference is called spin excess $\Delta \boldsymbol{N}$. In an external field $\vec{\boldsymbol{B}}_{\boldsymbol{0}}$, since the parallel and antiparallel spins cancel each other out, the spin excess $\Delta \boldsymbol{N}$ determines the net magnetic moment $\boldsymbol{M}_{\boldsymbol{0}}$ (Haidekker 2013), corresponding to the sum of all spin directions. By convention, the external magnetic field $\vec{\boldsymbol{B}}_{\boldsymbol{0}}$ is always considered to be oriented along the z-axis, and thus the net magnetic moment $\boldsymbol{M}_{\boldsymbol{0}}$ is also parallel to the z-axis. The net magnetic moment $\boldsymbol{M}_{\boldsymbol{0}}$ is thereby generally called longitudinal magnetization $\boldsymbol{M}_{\boldsymbol{z}}$ (Haidekker 2013).

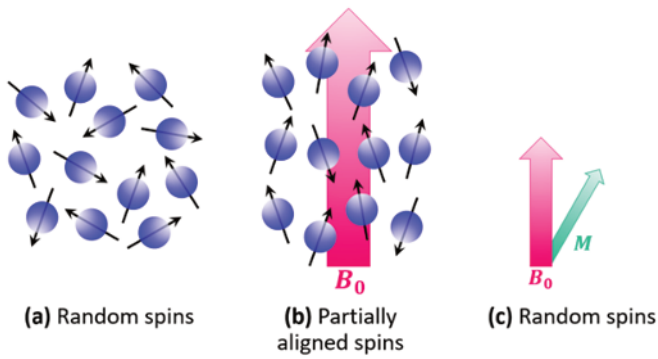

Figure 1.25. *Hydrogen atoms schematically represented by their axes of rotation: (a) randomly distributed in the absence of an external magnetic field, (b) partially aligned in the same direction as the applied magnetic field* $\vec{\boldsymbol{B}}_{\boldsymbol{0}}$*, owing to random interactions between the nuclei, and (c) with the accumulated magnetization* $\vec{\boldsymbol{M}}$ *of all the spins around* $\vec{\boldsymbol{B}}_{\boldsymbol{0}}$ *(Maier* et al. *2018)*

Moreover, the alignment of the axes of rotation of the hydrogen atom nuclei in relation to the direction of the magnetic field $\vec{B_0}$ is partial, owing to the random interactions between the nuclei (Figure 1.25). The spins obey the following movement equation (Haidekker 2013):

$$\frac{d\vec{M}}{dt} = \gamma\vec{M} \times \vec{B_0} \quad [1.4]$$

where γ is the gyromagnetic ratio. Therefore, γ determines the angular displacement and precession rate of the magnetic moment $\vec{M}$. It is important to highlight the inconsistency in the literature and between the different specialties regarding the definition and units of γ. Some authors call it the magnetogyric ratio and describe the gyromagnetic ratio as the reciprocal. Others treat it as a synonym for the Landé g-factor. The gyromagnetic ratio is sometimes expressed in $Hz\,T^{-1}$, causing a difference factor of 2π, or $s^{-1}\,T^{-1}$, which is ambiguous (Flower 2012).

At the beginning of the precession, the axis of rotation rotates around the direction of the magnetic field $\vec{B_0}$ according to a certain angle. This angle decreases over time, until the axis of rotation and the direction of $\vec{B_0}$ are aligned. This alignment is represented by the net magnetization vector $\vec{M}$. Due to the accumulation of hydrogen nuclei inside the body in the presence of a strong magnetic field $\vec{B_0}$, the net magnetization is proportional to the intensity of this field $\vec{B_0}$ (Maier *et al*. 2018).

The precession frequency f_l (also known as the Larmor frequency) of the nuclear spin depends on the intensity B_0 of the applied magnetic field and the gyromagnetic ratio γ (Maier *et al*. 2018):

$$f_l = \gamma B_0 \quad [1.5]$$

For hydrogen, the gyromagnetic ratio is approximately $42.58\,MHz/T$ and the precession frequency in a magnet of $1.5\,T$ is approximately $63.87\,MHz$ (Haidekker 2013). It should be noted that precession and rotation should not be confused (nucleus precession around the magnetic field direction and nucleus rotation around its own axis). In the following, only the net magnetization $\vec{M}$ will be considered.

When $\vec{M}$ is excited, i.e. moved from its initial equilibrium position, RF waves are emitted from the body. The direction of $\vec{M}$ changes when a weaker orthogonal magnetic field $\vec{B_1}$ to $\vec{B_0}$ is applied, with RF waves coming from a coil at the same resonant frequency as $\vec{M}$. The magnetic field $\vec{B_1}$ must, in fact, be orthogonal to $\vec{B_0}$ and its direction must be aligned with the direction of the present angle of rotation of $\vec{M}$ (Maier *et al*. 2018).

In order to better understand this phenomenon, a turntable is considered to be moving around the direction of the magnetic field $\vec{B_0}$ (Figure 1.26). The point of application of $\vec{M}$ is assumed to be on this turntable. Being based on a fixed inertial reference point, not belonging to the turntable, the movement of $\vec{M}$ follows a sort of spiral, since it has the same direction as the magnetic field $\vec{B_1}$ (Figure 1.26). If the reference point is fixed on the turntable, the direction of $\vec{B_1}$ becomes constant and the excitation induced by $\vec{B_1}$ can be differentiated, but the precession movement cannot be observed. By eliminating $\vec{B_1}$, $\vec{M}$ gradually returns to its equilibrium position through a process called relaxation, during which the RF waves emitted by the body are used to generate MRIs (Maier *et al*. 2018).

1.4.3. *Relaxation and contrast*

Relaxation refers to the return of net magnetization to its equilibrium state before excitation by an RF pulse. The rate of relaxation depends on the intensity of the applied magnetic field, as well as the tissues, owing to the limited interactions between protons in the case of large molecules or dense tissues characterized by an impeded movement of water molecules. The rate of relaxation therefore differs from one type of tissue to another. For instance, the water relaxation rate differs from the fat relaxation rate, hence the difference between the amounts of the received signal for each of them during the relaxation time. This is at the root of the tissue contrast in MRIs (Maier *et al*. 2018). Considering the microscopic origins of relaxation phenomena, NMR relaxation parameters are extremely sensitive indicators of the physical and chemical microenvironment, including nuclei of interest (Flower 2012).

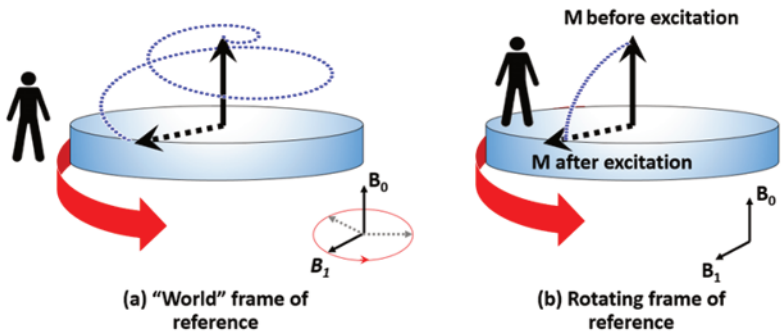

Figure 1.26. *Excitation and precession of the magnetization vector $\vec{M}$. This figure was reconstructed from Maier* et al. *(2018). For a color version of the figure, see www.iste.co.uk/benkahla/finite.zip*

A mathematical description of relaxation was first proposed by (Bloembergen *et al*. 1948). Other papers were subsequently published, providing a detailed description of relaxation physical principles and quantum mechanics (Abragam and Abragam 1961; Abragam 1983; Ernst *et al*. 1987; McConnell 1987; Levitt 2001; McConnell 2009). This section will provide a summary of these principles.

By considering a system of coordinates (o, x, y, z) and supposing that $\vec{B}_0$ is directed along the z-axis, each of the magnetization vectors can be divided into two components, a longitudinal $\vec{M}_z$ and a transverse $\vec{M}_{xy}$, such as $\vec{M} = \vec{M}_{xy} + \vec{M}_z$. Therefore, before relaxation, $\vec{M}_{xy} = 0$ and $\vec{M}_z \geq 0$. During excitation, an RF pulse moves the vector $\vec{M}$ tip towards the transverse plane, so that $\vec{M}_z = 0$ and $\vec{M}_{xy}$ is maximized. By deactivating the RF pulse, the spins regain their equilibrium state following, in general, two spin relaxation mechanisms: (1) a longitudinal relaxation, during which $\vec{M}_z$ tends to return to its initial intensity; and (2) a transverse relaxation, during which the intensity of $\vec{M}_{xy}$ tends towards 0. Hence, the intensity of $\vec{M}$ varies according to trajectory time, as shown in Figure 1.27 (Maier *et al*. 2018). Longitudinal relaxation is often called T_1 or "spin–lattice relaxation", where the term "lattice" implies a "thermal bath" of a well-defined temperature, to which each of the spin systems is independently coupled. T_1 results from the loss of proton energy in the ambient atmosphere (Flower 2012). The recuperation of $\vec{M}_z$ is actually expressed as $\vec{M}_z(t) = \vec{M}_0(1 - e^{\frac{-t}{T_1}})$. The relaxation T_1

describes the necessary time constant for $\vec{M}_z$ to recuperate $1-\frac{1}{e}$ ($\approx 63\%$) from its initial magnetization $\vec{M}_0$ (Maier *et al*. 2018). It corresponds to the energy transfer between the spin system and the network, modifying the magnetization longitudinal component (component z) (Flower 2012).

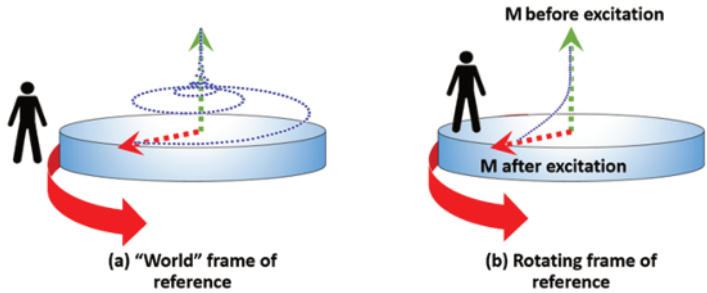

Figure 1.27. *Precession and relaxation of the white substance according to the two reference frames. Relaxation is represented by the blue trajectory, and the magnetization vector $\vec{M}_0$ (vector in green) turns towards the xy plane (vector in red). When relaxation begins, the length of the red vector ($\vec{M}_{xy}$) exponentially decreases with a speed defined by T_2. At the same time, the length of the green vector ($\vec{M}_{xy}$) increases at a speed defined by T_1. Moreover, the magnetization vector turns around the direction of the magnetic field $\vec{B}_0$ (direction of the z-axis) with the Larmor frequency dependent on the intensity of $\vec{B}_0$ (Maier* et al. *2018). For a color version of the figure, see www.iste.co.uk/benkahla/finite.zip*

The transverse relaxation is also called T_2 or "spin–spin relaxation", leading to two processes: the indirect exchanges using the network and the small differences between the precession frequencies between spins (Flower 2012), which result in a loss of magnetization perpendicularly to the outer field B_0 (Miller *et al*. 2014). In fact, $\vec{M}_{xy}$ is described by $\vec{M}_{xy}(t) = \vec{M}_0 e^{\frac{-t}{T_2}}$. T_2 corresponds to the time needed for $\vec{M}_{xy}$ to decrease following excitation to a value of $\frac{1}{e}$ ($\approx 37\%$) of its initial value $\vec{M}_0$ (Maier *et al*. 2018), describing the loss of magnetization in relation to the xy plane. This relaxation time depends on the tissue chemical structure and results in a slight modification of the nucleus effective field B_0, and therefore of the Larmor frequency. T_2 is always lower than T_1, and, for the majority of tissues, it is much faster than T_1 (Flower 2012).

The tight relationship between the relaxations T_1 and T_2 and the physical properties of the tissues of the region of interest create a tissue contrast.

Therefore, measuring the magnetic resonance signal during relaxation provides a contrast, resulting in images with different gray levels, whose intensities reflect the corresponding tissue densities. Changing the imaging parameters can lead to image "weighting", making it possible to reflect one type of relaxation more than another (Miller *et al*. 2014).

For a pulse sequence, two parameters are used to determine the way the resulting image will be weighted: (1) the echo time (ET) corresponds to the time period between the emission of an RF pulse and the peak of the echo signal; and (2) the repetition time (RT) corresponds to the time period between two successive RF pulses. Three main types of contrasts can therefore be identified: (1) the T_1 weighting of a short ET sequence as well as a short RT sequence, (2) the T_2 weighting of a long ET sequence as well as a long RT sequence, and (3) the proton density (PD) weighting of a short ET sequence and a long RT sequence. For example, liquids are generally characterized by long T_1 and T_2 and fats by short T_1 and T_2 (Miller *et al*. 2014). Consequently, a T_1 weighted image shows liquids in dark and fats in light, while a T_2 weighted image shows liquids in light and fats in dark (Figure 1.28).

The contrast or weighting selection in the MRI to be generated is of major importance, representing a determining factor of the subsequent medical application and therefore of its diagnostic importance (Maier *et al*. 2018). The majority of clinical exams are carried out with the images having T_1 weighting and T_2 weighting. Moreover, tissue abnormalities can be better defined by introducing a magnetic resonance contrast agent. Gadolinium is the most commonly used contrast agent. It is a paramagnetic agent that modifies the local magnetic field and considerably reduces the relaxation time T_1 of the neighboring water protons, which locally increases the signal on a T_1 weighted image (Miller *et al*. 2014).

1.4.4. *Applications of magnetic resonance imaging*

A number of MRI techniques have been developed over the last two decades, allowing its use in clinical trials for purposes of monitoring and assessment (Yu 2011).

1.4.4.1. *Diffusion-weighted imaging*

In water, molecules in continuous random motion, known as Brownian motion or Wiener process, induce isotropic diffusion that becomes anisotropic in the presence of structural components, such as cell membranes. This random molecular motion in water can be quantitatively measured using diffusion MRI. In basic diffusion-weighted imaging, the apparent diffusion coefficient is usually used to quantify water diffusion. When diffusion is restricted, for example in the case of ischemia, the apparent diffusion coefficient decreases and the signal on the diffusion-weighted imaging becomes clearer. This imaging modality is widely used in several therapeutic areas and is considered as an evaluation criterion in clinical trials (Miller *et al*. 2014).

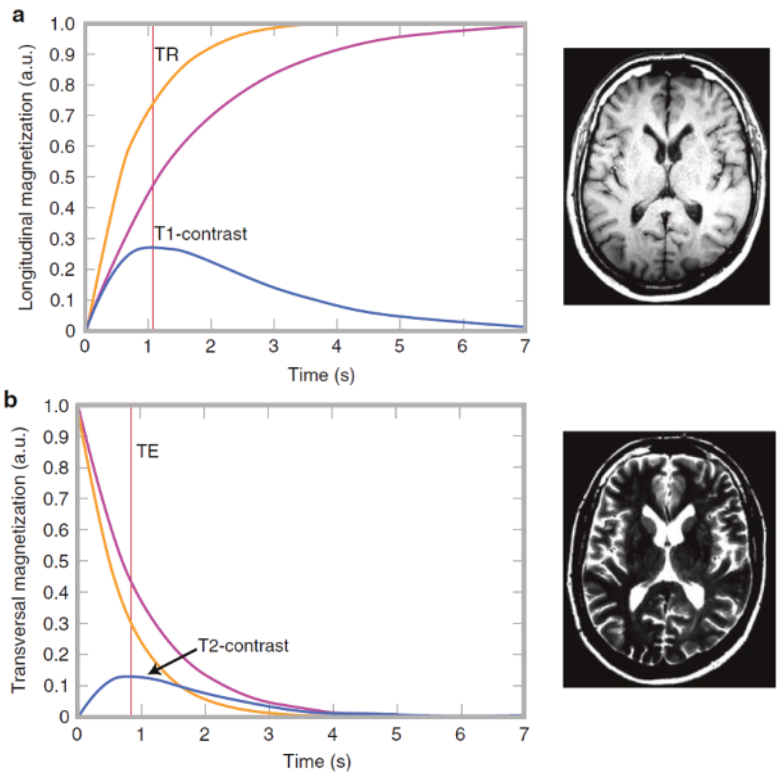

Figure 1.28. *Difference between the (a) T_1 and (b) T_2 weighted images of brain contrast (Scheef and Träber 2012). For a color version of the figure, see www.iste.co.uk/benkahla/finite.zip*

1.4.4.2. *Magnetic resonance spectroscopy*

Magnetic resonance spectroscopy is an imaging modality that can provide metabolic information from tissues *in vivo*, using the relationship between the resonance frequencies of nuclei and their chemical environment: a phenomenon known as chemical shift. Based on the anatomical reference images, MRS signals can be located on the volumes of interest of the targeted tissues. A magnetic resonance spectroscopy spectrum can be obtained by converting the signal acquired in the time domain into one in the frequency domain. For each spectrum peak, the resonance frequency position is determined based on the chemical shift. The resulting spectrum can be quantified either in standard signal strength or in absolute value.

Magnetic resonance spectroscopy is widely used for diagnosing and assessing response to treatment, as well as for neurological and hepatic studies. For example, the decrease in signal to a certain value reflects the decrease in a neural marker called NAA, indicating a neural loss or dysfunction (Miller *et al*. 2014).

1.4.4.3. *Functional magnetic resonance imaging*

Based on the fact that a region of the brain is more active when oxygen consumption is higher, functional MRI (fMRI) consists of measuring the degree of brain activity in relation to the level of oxygen consumed in each brain region using conventional MRI equipment. Indeed, the magnetic field generated by an MRI machine is able to detect the different concentrations of oxygenated and deoxygenated hemoglobin in the blood of the brain regions of interest. A color spectrum gradient is then produced, allowing the most active regions to be distinguished from the less active ones.

The fMRI also makes it possible to determine the most active region of an individual's brain when speaking or moving, or by using a variety of specific stimuli. This field has been the subject of several studies, leading to a significant evolution in the understanding of how the brain works during complex cognitive processes, such as deception (Mohamed *et al*. 2006).

1.4.5. *Advantages and disadvantages of magnetic resonance imaging*

The MRI technique also has its advantages and disadvantages, which are summarized in Table 1.3.

Advantages	Disadvantages
Possibility of providing slices according to the axial, sagittal and coronal planes	Relatively high cost
Detailed description of the contrast in soft tissues	Relatively limited availability
High sensitivity to fats and to small changes affecting them	Longer than average length of examination
Non-invasive, non-ionizing and non-contrast iodinated technique	Limited sensitivity to detecting calcification and periosteal reaction
No side effects for children or pregnant women	Contraindications in the presence of ferromagnetic aneurysm forceps, metal foreign bodies in orbits, pacemakers, cochlear implants, insulin pumps and other electronic implants, as well as in the case of severe renal failure or dialysis
Multi-plane and multi-parametric examination	Frequent appearance of artifacts during relatively long imaging sequences

Table 1.3. *Advantages and disadvantages of MRI (Ceniccola* et al*. 2018)*

1.5. Ultrasound imaging

Acoustic waves can be classified into three categories: (1) infrasound, in the subsonic range, with a frequency of less than 16 Hz, (2) acoustic sound, in the audible range that can be detected by the human auditory system, with a frequency between 16 Hz and 20 kHz, and (3) ultrasound, with a frequency exceeding 20 kHz. The latter category is used in several applications ranging from measuring distances at sea to medical applications.

1.5.1. *Definition of ultrasound*

Ultrasound refers to sound waves with frequencies exceeding 20 kHz (Figure 1.29). This form of mechanical energy can be used to create medical images of different body parts, including muscles, blood vessels and soft tissues, due to its balanced penetration and interaction with the body. Ultrasound is reflected and refracted at the interface level separating media with different acoustic refractive indices (Flower 2012; Cikes *et al*. 2017).

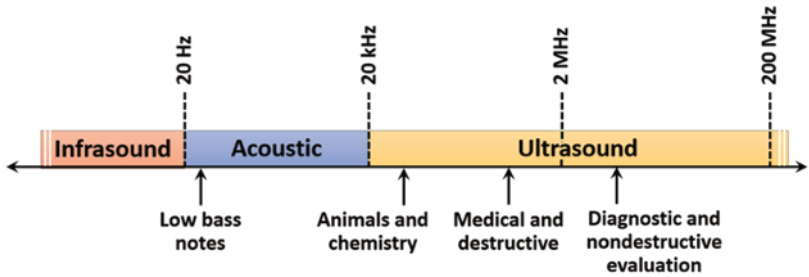

Figure 1.29. *Acoustic wave spectrum (Mikla and Mikla 2013). For a color version of the figure, see www.iste.co.uk/benkahla/finite.zip*

As with all other types of wave, ultrasound is mainly characterized by the frequency $\boldsymbol{F}$, the speed $\boldsymbol{v}$, the wavelength $\boldsymbol{\lambda}$ and the intensity $\boldsymbol{J}$. Typically, ultrasound intensity used for diagnosis varies from 1 to 10 mW m^{-2}. It should be recalled that the wavelength $\boldsymbol{\lambda}$ is linked to the frequency $\boldsymbol{F}$ and the speed of sound $\boldsymbol{c}$ according to the fundamental wave equation:

$$\boldsymbol{\lambda} = \frac{\boldsymbol{c}}{\boldsymbol{F}} \qquad [1.6]$$

Owing to the significant attenuation of high frequencies in tissues, the different body parts are examined using different frequencies ranging from 3 to 5 MHz for abdominal areas, from 5 to 10 MHz for superficial parts and small sizes, and from 10 to 30 MHz for eyes and skin (Mikla and Mikla 2013).

1.5.2. *Development of ultrasound imaging*

The development of ultrasonography dates back to the 21st Century BCE, owing to the study carried out by the Roman architect and engineer Vitruvius on the acoustics of theaters, in which interference, echoes and reverberation were discussed. The application of ultrasonography in medicine began with the first description of the influence of sound waves through liquids, in 1927, by Robert Williams Wood and Alfred Lee Loomis. In the 1930s, Karl Theodore Dussik and his brother began studying the human brain using sonograms (Figure 1.30) (Christian *et al*. 2014). Today, ultrasound is frequently used in medicine for diagnostic purposes, at frequencies typically ranging from 2 to 40 MHz. However, these sound waves are now undergoing a development, making it possible to use them in therapeutic applications (Maier *et al*. 2018).

1.5.3. *Generation of ultrasound*

Mechanical pressure can be converted into an electrical voltage (piezoelectric effect) using piezoelectric crystals or materials. This electrical voltage can be measured with two electrodes (Figure 1.31). Conversely, applying electrical energy to a piezoelectric crystal (indirect or reciprocal piezoelectric effect) causes the mechanical distortion of the crystal, leading to its vibration and to the generation of sound waves. This is the basic principle of ultrasound generation from transducers (Mikla and Mikla 2013; Sehmbi and Perlas 2015).

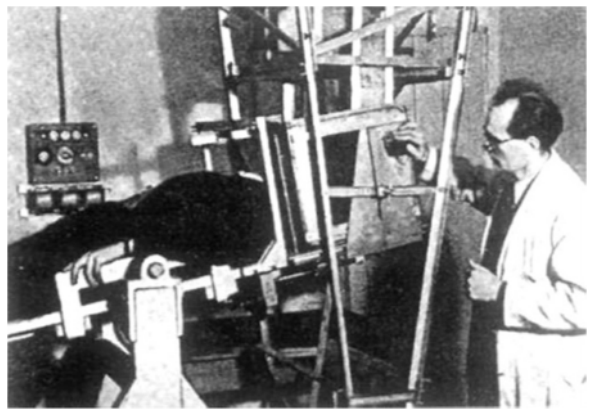

Figure 1.30. *Karl Dussik and his ultrasound apparatus in 1946 (Christian* et al. *2014)*

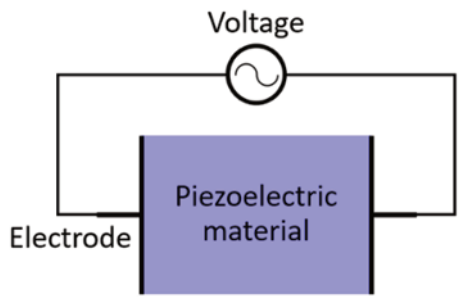

Figure 1.31. *Piezoelectric effect (Maier* et al. *2018)*

Typically, barium titanate (BaTiO3) and lead zirconate titanate (PZT) are used as piezoelectric materials (Maier *et al*. 2018).

1.5.4. *Transducers*

An ultrasonic transducer plays the role of both a generator and a detector of ultrasonic waves. It converts mechanical energy into electrical energy, and vice versa. As they penetrate, ultrasound echoes are generated by reflection and diffusion, following their contact with tissues and body fluids. Using the characteristics of these echoes and depending on the type of the used transducer, 1D, 2D or 3D images of the regions of interest can be reconstructed and visualized (Maier *et al*. 2018).

1.5.4.1. *Conventional construction (single-element transducers)*

The main components of a single-element transducer are shown in Figure 1.32.

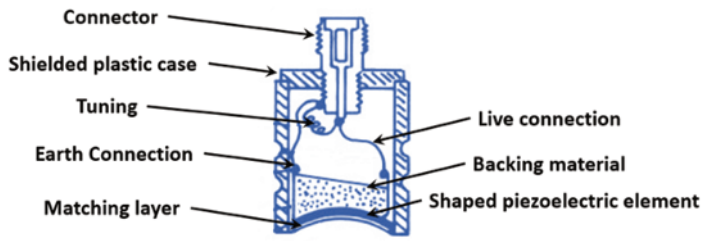

Figure 1.32. *Typical components of a conventional single-element transducer (Flower 2012)*

The piezoelectric element is cut and generally shaped from a piezoelectric ceramic (usually lead zirconate titanate, PZT) or plastic (polyvinylidene difluoride, PVDF). Electrodes, made of silver, are deposited on both the front and back faces, with a permanent polarization of the element across its thickness. Therefore, applying a voltage across these electrodes induces a proportional change in thickness, and applying a pressure across the two faces induces a difference in potential between the electrodes. Focusing can be applied by several methods: a shaped concave ceramic, a lens plus a plane ceramic disk, a bowl plus a defocusing lens, as well as overlapping beams from two elements (Flower 2012).

To overcome acoustic mismatching between the element and the tissue, a matching layer is applied, thereby allowing the increase in the energy transfer efficiency. However, this is only applicable in the case of continuous waves, where the ideal layer thickness and impedance are respectively (Flower 2012):

$$T_{matching} = \frac{\lambda}{4} \quad [1.7]$$

$$Z_{matching} = (Z_{element} \times Z_{tissue})^{\frac{1}{2}} \quad [1.8]$$

It should be mentioned that PVDF elements do not require a matching layer.

A backing medium is usually used to provide mechanical support. However, it should be minimal if maximum efficiency is desired. In addition, single-element transducers are also composed of a casing that should be electrically screened and acoustically decoupled from the element, in order to prevent dynamic range reduction caused by electrical interference or acoustic ringing. Electrical tuning is frequently used to filter out the element's low frequency radial mode vibrations, as well as to manipulate the electrical amplitude parameters, in order to provide the best compromise between resolution and sensitivity. The transducer element capacitance is expressed as follows (Flower 2012):

$$C_t = \frac{\varepsilon A_t}{T} \quad [1.9]$$

where ε is the element dielectric constant and A_t is the element area.

Although the same basic design aspects of the conventional construction are maintained, modern scanning equipment is based on using multiple-element transducers rather than single-element ones (Flower 2012).

1.5.4.2. *Multiple-element transducers*

As their name indicates, multiple-element transducers involve more than one element to enable the use of continuous waves, where separate transmitting and receiving elements are required. The general principle is based on simultaneously exciting a group of tiny elements (piezoelectric crystals), making it possible to produce a plane wavefront emerging from the aperture formed by the spatial extent of these elements. Then, the excitation of a different, but overlapping, group of elements induces the translation of the sound beam from position 1 to position 2 (Figure 1.33a). Focusing or steering the sound beam requires exciting each element via a variable delay. Ultrasound systems, operating based on this technology, are known as "phased-array" systems, creating a sector-shaped image by phase steering the sound beam (Flower 2012).

Receive beam formation consists of (1) selecting an array element group that will form the desired acoustic receiving aperture, (2) applying a variable delay to the signal received on each element and (3) summing the signals over all the elements in the group. Therefore, a single receive beam line is formed. Owing to the delays on transmission, the synthetized beam is steered and focused to a given angle and distance (Figure 1.33b and 1.33c). Then, a receiver is generated with a maximum sensitivity to echoes arriving from that focal distance and steering direction. Indeed, during the time that a complete sequence of echoes takes to return, following a single transmitted sound pulse, the focusing delays may be continuously adjusted, in order to maximize the sensitivity, and thus the focusing of the system receiving directivity pattern on the position of each echo when arriving from each depth. This is known as swept or dynamic focusing approach, which is only applied to the received signal. Modifications in the transmitted beam focal properties can only be made over successive sound pulses, by applying a different delay combination on each pulse (Flower 2012).

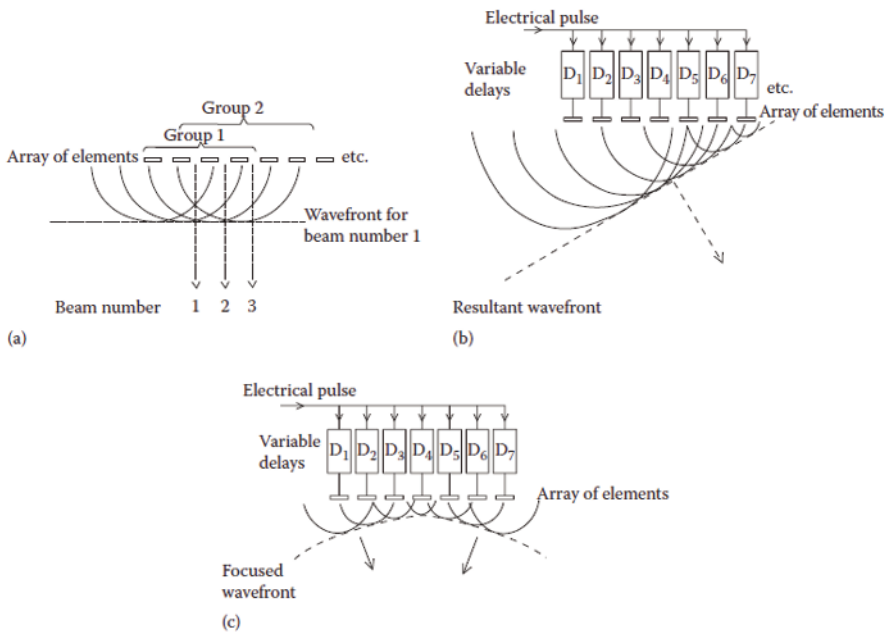

Figure 1.33. *Schematic 2D representation of the principles of beam forming (a–c), focusing (c), lateral scanning (a) and steering (b), using arrays of elemental sound sources (Flower 2012)*

1.5.5. *Applications of ultrasound techniques*

Given the very broad use of ultrasound imaging, this brief overview only focuses on presenting its main applications.

1.5.5.1. *Grayscale imaging*

The use of this imaging modality in grayscale is very widespread.

1.5.5.1.1. Brain

In adults, ultrasound is not able to visualize the brain anatomy, because of the attenuation and refraction properties of the skull, although several brain disorders, such as Parkinson's disease, have recently been depicted. However, ultrasound imaging can be used for intraoperative guidance in neurosurgery carried out on adults, although less frequently than MRI and CT (Flower 2012). In newborns, the brain can be visualized due to the anterior fontanelle (Figure 1.34), allowing several conditions to be diagnosed during the first months of life (Suetens 2009).

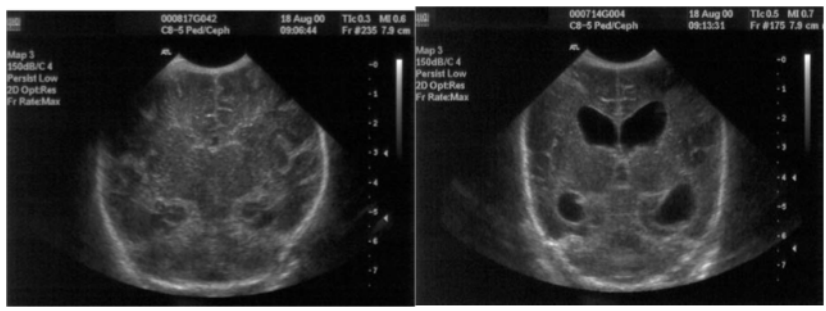

Figure 1.34. *Ultrasound imaging showing a normal skull (left) and fluid-filled cavities on both sides following intraventricular hemorrhage (right) (Suetens 2009)*

1.5.5.1.2. Eye and orbital

The small size of ocular and eye socket (or orbital) structures requires high resolution without deep penetration. Therefore, equipment has been specifically designed for ophthalmic use (Figure 1.35), with frequencies typically ranging from 13 to 20 MHz, but reaching up to 50 MHz for some applications, such as biometry. This imaging modality makes it possible to measure the eye axial length and to accurately determine the reflective

interface location. In addition, information on eye movement and topography can be obtained (Flower 2012).

Transducers of 20 MHz may be used to image the retina (Figure 1.36). This type of wave provides limited penetration depth because of their high attenuation coefficient. This loss of acoustic energy is however negligible for surface tissues, such as the retina (Suetens 2009).

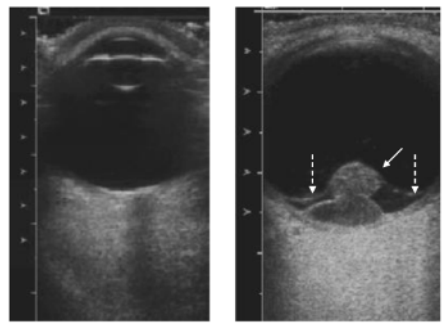

Figure 1.35. *Ophthalmic ultrasound showing (left) a normal eye and (right) a collar button-shaped malignant melanoma in the shape of a "collar" (solid arrow) with a detachment of the overlying retina (dotted arrows) (Flower 2012)*

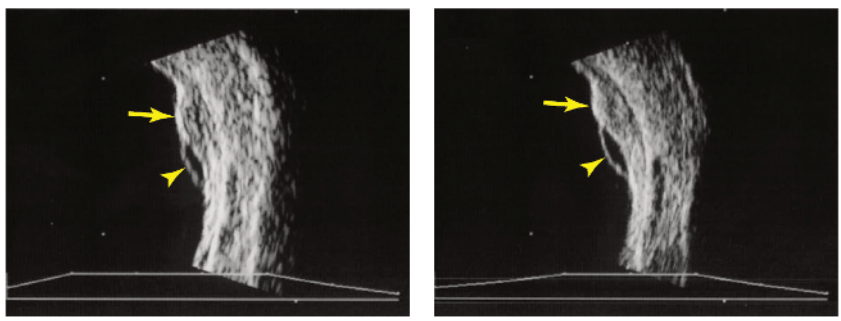

Figure 1.36. *Ultrasound image of an eye showing a malignant melanoma at the top (arrow) and a localized detachment of the retina at the bottom (arrow head), using a 10 MHz (left) and 20 MHz (right) scan (Suetens 2009)*

1.5.5.1.3. Neck

Soft superficial tissues, such as the thyroid (Figure 1.37), lymph nodes and salivary glands, can be easily imaged using ultrasound (Suetens 2009).

In the thyroid, functional studies of radionuclides can be supplemented by structural information obtained using ultrasound, which mainly contributes by differentiating solid and cystic nodules (Flower 2012).

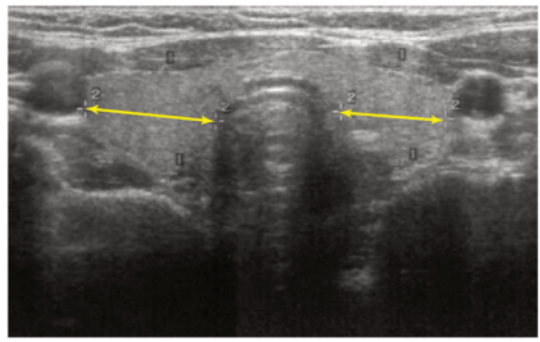

Figure 1.37. *Thyroid ultrasound showing a slight bilateral enlargement (arrows), suggesting a hormonal imbalance or an inflammatory disease (Suetens 2009)*

1.5.5.1.4. Fetus and gynecology

For pregnant women, ultrasound imaging has become a normal routine, enabling the acquisition of information on the fetus (Figure 1.38), the uterus and the placenta (Suetens 2009). It has also become the preferred method for studying the female pelvis. Gynecological examinations can be performed with transabdominal techniques using a full bladder as an acoustic window, or with transvaginal techniques that can be combined with sonohysterography, where a catheter is passed through the cervix to the uterine cavity by gently injecting a sterile saline solution, thus providing an excellent delimitation of the endometrial cavity and facilitating the diagnosis of structural and morphological anomalies (Flower 2012).

1.5.5.2. *Doppler ultrasound*

Doppler ultrasound is based on a phenomenon familiar to train enthusiasts: by standing beside railroad tracks when a train is whistling while moving rapidly, the pitch of the whistle increases as the train approaches and becomes lower as the train passes by the observer and speeds off into the distance. The variation in the whistle pitch results from the Doppler effect, which consists of an apparent change in the sound frequency. The same phenomenon occurs at ultrasound frequencies, and the Doppler effect is used to determine the direction and measure the speed of blood flow. For a

grayscale image of the region of interest, the blood flow is displayed in red in one direction and in blue in the other direction (Figure 1.39) (Bushberg and Boone 2011).

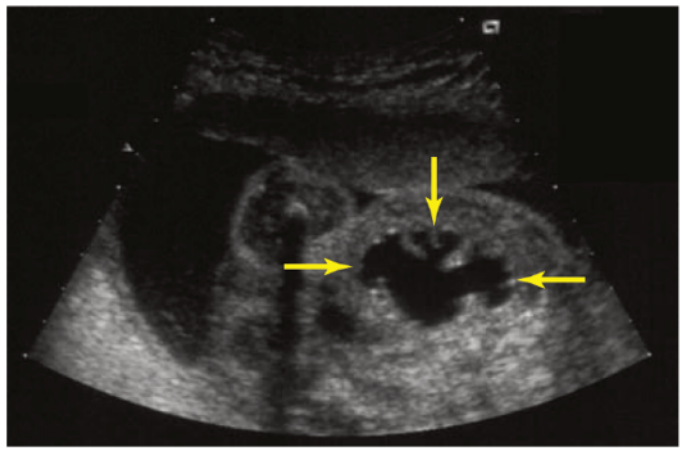

Figure 1.38. *Transverse ultrasound of a fetus abdomen, showing a fluid-filled and dilated left kidney collection system (arrows) caused by the kidney outlet obstruction (Suetens 2009)*

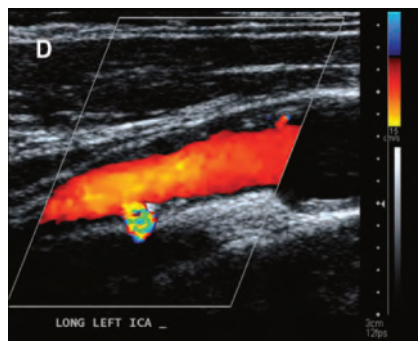

Figure 1.39. *Doppler color flow imaging used for vascular assessment. The color flow can be obtained by many ultrasound systems. This figure shows an internal carotid artery superimposed on the grayscale image, showing an aneurysm in the left internal carotid artery (Bushberg and Boone 2011). For a color version of the figure, see www.iste.co.uk/benkahla/finite.zip*

1.5.5.3. *Echocardiography*

Echocardiography is used to evaluate cardiac movements and structures by inserting a probe into the esophagus (transesophageal echocardiography (Figure 1.40) via the surface of the chest wall (transthoracic echocardiography). A beam, or varying ultrasound beams, produces an image or video showing the heart wall, vascular system and valves, as well as the movements of these different structures during blood pumping. Pathologies, such as fluid accumulation around the heart and valve regurgitation, can therefore be determined. Furthermore, a 3D echocardiography can be performed using a set of multiple transducers with an advanced processing system that allows a 3D visualization of the heart in several planes (Miller *et al*. 2014).

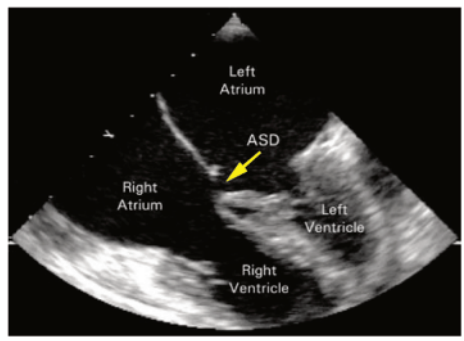

Figure 1.40. *Transesophageal echocardiography showing an atrial septal defect (Suetens 2009)*

1.5.5.4. *Bone ultrasonometry*

Bone ultrasound was developed in the 1980s to evaluate osteoporosis. Unlike the ultrasound imaging modalities described above, this modality is based on a transmission at a nominal frequency of 1 MHz or lower, producing a sufficient measurement signal with attenuation correlated with bone quantity and quality. Most systems are able to assess the calcaneus and measure broadband ultrasound attenuation (BUA) from 0.2 to 0.6 MHz or the speed of sound (SOS) through the bone. However, the accuracy of this modality is lower than that of DXA; hence, bone ultrasonometry is acceptable for clinical trials (Miller *et al*. 2014).

1.5.6. *Advantages and disadvantages of ultrasound imaging*

Similar to all other medical imaging techniques, ultrasound imaging has advantages and disadvantages, which are summarized in Table 1.4.

Advantages	Disadvantages
Ability to provide real-time information	Agreement and clinical protocol paucity on their use
No required special infrastructure	Technique limited by situations of excessive edema
Wide availability	Little contribution to the assessment of bone tumors
Portability	Inability to entirely visualize intraosseous lesions
Low cost	Inability to penetrate adult cortical bone
Non-invasive and non-ionizing technique	
Ability to evaluate changes in longitudinal muscle	

Table 1.4. *Advantages and disadvantages of ultrasound imaging technique (Ceniccola* et al. *2018)*

1.6. Comparison between the different medical imaging techniques

Medical imaging techniques can be compared in terms of three major concepts. The first concept is image quality, which can be represented by (1) contrast, referring to the difference in brightness or darkness of the image between a region of interest and its background; (2) spatial resolution, referring to the spatial extent of small objects in the image; and (3) noise, referring to the accuracy with which the signal is received. The second concept is the system availability, which can be represented by its cost and its ability to provide real-time information. The third concept is safety, involving the effects of ionizing radiation and heat on the body (Kasban *et al*. 2015).

Table 1.5 summarizes and compares the different medical imaging techniques detailed above.

Imaging technique	Image quality		Availability of the system		Safety	
	Spatial resolution	Good contrast	Cost	Real-time information	Ionizing radiation	Heating effect
Radiography	1 mm	Soft tissues and fluid	Average	No	Yes	Low
CT	0.5 mm	Hard tissues and fluid	High	No	Yes	Low
MRI	0.5 mm	Hard tissues and fluid	High	No	No	Average
Ultrasound	1 mm	Soft tissues	Low	Yes	No	Negligible

Table 1.5. *Comparison between medical imaging techniques (Kasban* et al. *2015)*

1.7. Conclusion

Medical imaging has been broadly developed to be a particularly effective and necessary technique for clinical care among medical professionals. The multiple existing modalities have offered numerous advantages spurring the use of medical imaging as an eligibility requirement, as well as a biomarker in clinical trials for several endpoints for efficacy and safety. Nevertheless, each technique has its advantages and its limitations and counter-indications. Therefore, none of them can be reliable individually in all medical applications.

While this chapter addresses the basic physics of the main medical imaging techniques, the next chapter focuses on the major steps and methods used in processing the generated medical images, in order to create digital models of the different organs and tissues in the human body.